

# Geophysical Research Letters

## RESEARCH LETTER

10.1029/2019GL084630

### Key Points:

- High-quality, inclusion-free bridgmanite single crystals ( $\text{Mg}_{0.88}\text{Fe}^{3+}_{0.065}\text{Fe}^{2+}_{0.035}\text{Al}_{0.14}\text{Si}_{0.90}\text{O}_3$ ) were synthesized and characterized
- The crystals contain  $\sim 1,020(\pm 70)$  ppm wt water using NanoSIMS and show pronounced OH-stretching bands at  $\sim 3230$  and  $\sim 3460\text{ cm}^{-1}$  in FTIR spectra
- Dehydration melting at the topmost lower mantle can occur when water content exceeds  $\sim 0.1$  wt% solubility limit

### Supporting Information:

- Supporting Information S1
- Data Set S1

### Correspondence to:

J.-F. Lin and S.-i. Karato,  
afu@jsg.utexas.edu;  
shun-ichiro.karato@yale.edu

### Citation:

Fu, S., Yang, J., Karato, S.-i., Vasiliev, A., Presniakov, M. Y., Gavriiliuk, A. G., et al. (2019). Water concentration in single-crystal (Al,Fe)-bearing bridgmanite grown from the hydrous melt: Implications for dehydration melting at the topmost lower mantle. *Geophysical Research Letters*, 46. <https://doi.org/10.1029/2019GL084630>

Received 19 JUL 2019

Accepted 12 AUG 2019

Accepted article online 16 AUG 2019

## Water Concentration in Single-Crystal (Al,Fe)-Bearing Bridgmanite Grown From the Hydrous Melt: Implications for Dehydration Melting at the Topmost Lower Mantle

Suyu Fu<sup>1</sup> , Jing Yang<sup>1,2</sup> , Shun-ichiro Karato<sup>3</sup> , Alexander Vasiliev<sup>4,5,6</sup>, Mikhail Yu. Presniakov<sup>4</sup>, Alexander G. Gavriiliuk<sup>6,7,8</sup> , Anna G. Ivanova<sup>6,7</sup> , Erik H. Hauri<sup>9,10</sup> , Takuo Okuchi<sup>11</sup> , Narangoo Purevjav<sup>11</sup> , and Jung-Fu Lin<sup>1</sup> 

<sup>1</sup>Department of Geological Sciences, Jackson School of Geosciences, The University of Texas at Austin, Austin, TX, USA,

<sup>2</sup>Geophysical Laboratory, Carnegie Institution of Washington, Washington, DC, USA, <sup>3</sup>Department of Geology and Geophysics, Yale University, New Haven, CT, USA, <sup>4</sup>National Research Center, Kurchatov Institute, Moscow, Russia,

<sup>5</sup>Moscow Institute of Physics and Technology, Moscow, Russia, <sup>6</sup>Shubnikov Institute of Crystallography of Federal Scientific Research Center Crystallography and Photonics, Russian Academy of Sciences, Moscow, Russia, <sup>7</sup>Institute for Nuclear Research, Russian Academy of Science, Moscow, Russia, <sup>8</sup>REC Functional Nanomaterials, Immanuel Kant Baltic Federal University, Kaliningrad, Russia, <sup>9</sup>Department of Terrestrial Magnetism, Carnegie Institution of Washington, Washington, DC, USA, <sup>10</sup>Deceased, <sup>11</sup>Institute for Planetary Materials, Okayama University, Misasa, Japan

**Abstract** High-quality single-crystals of (Al,Fe)-bearing bridgmanite,  $\text{Mg}_{0.88}\text{Fe}^{3+}_{0.065}\text{Fe}^{2+}_{0.035}\text{Al}_{0.14}\text{Si}_{0.90}\text{O}_3$ , of hundreds of micrometer size were synthesized at 24 GPa and 1800 °C in a Kawai-type apparatus from the starting hydrous melt containing  $\sim 6.7$  wt% water. Analyses of synthesized bridgmanite using petrographic microscopy, scanning electron microscopy, and transmission electron microscopy show that the crystals are chemically homogeneous and inclusion free in micrometer- to nanometer-spatial resolutions. Nanosecondary ion mass spectrometry (NanoSIMS) analyses on selected platelets show  $\sim 1,020(\pm 70)$  ppm wt water (hydrogen). The high water concentration in the structure of bridgmanite was further confirmed using polarized and unpolarized Fourier-transform infrared spectroscopy (FTIR) analyses with two pronounced OH-stretching bands at  $\sim 3,230$  and  $\sim 3,460\text{ cm}^{-1}$ . Our results indicate that lower-mantle bridgmanite can accommodate relatively high amount of water. Therefore, dehydration melting at the topmost lower mantle by downward flow of transition zone materials would require water content exceeding  $\sim 0.1$  wt%.

**Plain Language Summary** Water cycle between surface oceans and Earth's deep interior is a key to understanding the evolution and physical/chemical states of the planet. Early studies show that major transition zone minerals, wadsleyite, and ringwoodite, could accommodate abundant water (1–3 wt%), in the form of lattice-bonded hydrogen atoms, in their crystal structures. However, water solubility in lower-mantle bridgmanite, the most abundant mineral in the most volumetric layer of the planet, has remained poorly understood. The scientific challenge here was largely due to difficulties in making large-sized high-quality single-crystals of bridgmanite for reliable characterizations of its water concentration. Here we synthesized single-crystal bridgmanite of a few hundred micrometers in diameter, which are examined to be inclusion and precipitate free and thus can be used for reliable water concentration measurements using NanoSIMS analyses. Unpolarized and polarized FTIR analyses are used to identify characteristic OH-stretching bands. Our results show that (Al,Fe)-bearing bridgmanite could contain as high as  $1,020(\pm 70)$  ppm wt water. This high water concentration in bridgmanite has implications for our understanding of how melting can occur deep in the mantle below the transition zone.

## 1. Introduction

Water (hydrogen) can be dissolved into the structures of most mantle minerals including those that nominally do not have hydrogen in their chemical formulae such as olivine and its high-pressure polymorphs, wadsleyite, and ringwoodite,  $(\text{Mg,Fe})_2\text{SiO}_4$ , called as nominally anhydrous minerals (NAMs; e.g., Bolfan-Casanova, 2005; Karato, 2015; Peslier et al., 2017). Water in NAMs can have significant effects on a variety of properties, including melting relationships (Inoue, 1994; Kawamoto, 2004), rheological properties (Karato & Jung, 2003; Mei & Kohlstedt, 2000), and electrical conductivity (Karato & Wang,

2013). For instance, early studies indicate that partial or dehydration melting would occur when water-rich materials in the transition zone such as wadsleyite or ringwoodite are transported to either upper or lower mantle regions where water solubility is low (e.g., Bercovici & Karato, 2003; Liu et al., 2016; Schmandt et al., 2014; Tazuin et al., 2010). When melting occurs, a majority of water would strongly partition into the melt. Since the melt is generally mobile, melting near the transition zone regions could lead to large-scale transport of water in the Earth's mantle. Therefore, understanding the behavior of hydrogen in mantle minerals is important for our knowledge of the dynamics and evolution of the Earth.

A major goal of previous work has been to determine the solubility of water in mantle NAMs at various pressures, temperatures, and oxidation states. There has been a reasonable agreement on research results for upper mantle and transition zone minerals (e.g., Karato, 2015; Ohtani, 2015; Peslier et al., 2017). However, water solubility in the lower-mantle minerals, particularly for bridgmanite, has been poorly constrained. Previous studies suggested that bridgmanite can contain either low (a few ppm wt, near or less than the detection limit) or high (~2,000 ppm wt) water concentrations (e.g., Bolfan-Casanova et al., 2003; Inoue et al., 2010; Litasov et al., 2003; Meade et al., 1994; Murakami et al., 2002; Panero et al., 2015). Consequently, the conditions at which melting would occur at the topmost lower mantle by downward flow of transition zone minerals are not well constrained.

The cause of large variations in reported water concentrations in bridgmanite is not well known but includes differences in synthesis conditions at high pressure-temperature (P-T), compositions and water contents of starting materials, and quenching rates; the use of different analytical techniques and their calibrations; total Fe, Al as well as  $\text{Fe}^{3+}$  contents in bridgmanite; and possible contaminations from inclusions of hydrous phases and/or precipitates (e.g., Kaminsky, 2018). In the next two sections, we will present a review to identify possible causes for different results on water solubility in bridgmanite from previous studies. The potential role of inclusions on reported results is emphasized in the discussion below.

### 1.1. The Use of Analytical Techniques

In order to characterize water in mantle minerals, Fourier-transform infrared spectroscopy (FTIR) and secondary ion mass spectrometry (SIMS) have been commonly used (e.g., Pearson et al., 2014; Sambridge et al., 2008). FTIR can be used to detect characteristic structural OH absorption bands typically in the range of  $3,000\text{--}3,800\text{ cm}^{-1}$ . The main advantage of FTIR is that the nature of hydrogen-related species can be inferred from the frequencies of absorption. Consequently, absorption by inclusions and/or surface contaminants could be distinguished from absorption by hydrogen dissolved in crystallographic sites of the candidate crystals. To estimate hydrogen content from IR absorption, one needs reliable calibrations of absorption coefficients in specific crystallographic orientations relative to the polarization direction of the IR beam (Asimow et al., 2006; Aubaud et al., 2007; Balan et al., 2008; Paterson, 1982). However, this calibration standard has not been established yet for bridgmanite. In contrast, SIMS can be used to measure bulk water contents (e.g., Hauri et al., 2011; Kumamoto et al., 2017; Mosenfelder et al., 2011). Nevertheless, in SIMS analyses one cannot distinguish hydrogen in inclusions (e.g., glasses and secondary phases), precipitates, and surface contaminants (e.g., hydroxyls) from hydrogen in crystalline lattices of the sample, if one of these sources is present.

### 1.2. The Role of Inclusions

Experiments on water partitioning between ringwoodite and bridgmanite using multianvil apparatus found that water preferentially partitions into ringwoodite, and ~1–2 ppm wt water was reported to be barely detectable in  $\text{MgSiO}_3$  or Fe-bearing bridgmanite using FTIR analysis (Bolfan-Casanova et al., 2000; Bolfan-Casanova et al., 2003). The synthesized single-crystal bridgmanite was in coexistence with hydrogen-rich ringwoodite and contained numerous tiny inclusions of super hydrous phase B and brucite (Bolfan-Casanova et al., 2000; Bolfan-Casanova et al., 2003; Inoue et al., 2010). Furthermore, recent experiments suggested that bridgmanite synthesized from both hydrous and dry enstatite in laser-heated diamond anvil cells contained less than 220 ppm wt water (Panero et al., 2015). The synthesized bridgmanite coexisted with polycrystalline stishovite, Pt metal (as a laser absorber), and melt (Panero et al., 2015). We should note that FTIR technique does not have the spatial resolution to distinguish water in bridgmanite from these coexisting phases. Water may have strongly partitioned into stishovite and/or Pt metal (Litasov et al., 2007; Schwager et al., 2004; Spektor et al., 2011), lowering the amount of water in bridgmanite below what

is possible for bridgmanite coexisting with hydrous melt. In contrast to these studies, high water concentration, as much as 0.2 wt%, was reported in (Al,Fe)-bearing bridgmanite using FTIR and SIMS analyses (Murakami et al., 2002). However, Schmandt et al. (2014) observed the formation of intergranular melt around bridgmanite grown from hydrous ringwoodite, and the intergranular melt displayed the same FTIR spectra as observed by Murakami et al. (2002). This indicated that the high water solubility of ~0.2 wt% reported by Murakami et al. (2002) was likely due to the presence of intergranular hydrous melt inclusions between grain boundaries. We note that the IR spectra of ferropericlaase and bridgmanite collected by Murakami et al. (2002) are almost identical with a broad band at 3,200–3,600  $\text{cm}^{-1}$ , suggesting possible contaminations from hydrous melt inclusions. On the other hand, Litasov et al. (2003) reported 100 ppm wt water in  $\text{MgSiO}_3$  bridgmanite from FTIR measurements. Their studies further indicated that Al-bearing bridgmanite exhibits significantly higher water solubility as a result of Al substitution induced vacancies in the lattice: bridgmanite containing 4–7 wt%  $\text{Al}_2\text{O}_3$  can contain as high as 1,000–1,500 ppm wt water (Litasov et al., 2003). Furthermore, (Al,Fe)-bearing bridgmanite in various mantle rock types can contain different amounts of water (Litasov et al., 2003): the water concentration was suggested to be 40–110 ppm wt in the MORB system ( $\text{Al}_2\text{O}_3 = 13\text{--}17$  wt%,  $\text{Fe}/(\text{Fe} + \text{Mg}) = 0.39\text{--}0.42$ ) and 1,400–1,800 ppm wt in the peridotite system ( $\text{Al}_2\text{O}_3 = 5\text{--}6$  wt%,  $\text{Fe}/(\text{Fe} + \text{Mg}) = 0.1\text{--}0.12$ ). Litasov et al. (2003) also reported hydrous mineral inclusions in thick samples. Some sharp absorption peaks overlaid the broad bands in their IR spectra, which might be indicative of contaminants.

In summary, we believe the presence of hydrogen-rich inclusions is the most serious cause for the discrepancy of previous results on water concentration in bridgmanite. The origins of inclusions are not well understood but include the fast crystal growth or formation of precipitates during temperature quenching. We should note that if a bridgmanite sample contains hydrogen-rich inclusions (melt, super hydrous phase B, etc.), the water concentration in inclusion-free regions is controlled by water partitioning between the clean and inclusion-rich regions. Because hydrogen preferentially partitions into hydrogen-rich phases, the reported water concentration from such a sample will be strongly biased. Consequently, the results in early bridgmanite samples with inclusions cannot truly reflect its water solubility under relevant lower-mantle P-T and compositional conditions where hydrogen-rich phases do not exist. In order to obtain robust water solubility in bridgmanite, it is essential to synthesize high-quality bridgmanite crystals without inclusions/contaminants and characterize them carefully using multiple analytical techniques.

Here we synthesized large-size single-crystal (Al,Fe)-bearing bridgmanite,  $\text{Mg}_{0.88}\text{Fe}^{3+}_{0.065}\text{Fe}^{2+}_{0.035}\text{Al}_{0.14}\text{Si}_{0.90}\text{O}_3$ , using a Kawai-type apparatus at 24 GPa and 1800 °C with a heating duration of 20 hr. In order to characterize its quality, including (1) homogeneity of major element chemistry; (2) amount of  $\text{Fe}^{3+}$ ; (3) presence or absence of inclusions and/or precipitates, we used electron microprobe analysis (EPMA), scanning electron microscopy-energy dispersive spectroscopy (SEM-EDS) mapping, transmission electron microscopy (TEM) including high-resolution TEM (HRTEM) images, X-ray diffraction (XRD) and micro-Raman spectroscopy analyses. The crystals are examined to be chemically homogeneous and inclusion free in micrometer- to nanometer-spatial resolution. NanoSIMS measurements show the (Al,Fe)-bearing bridgmanite contains ~1,020( $\pm$ 70) ppm wt water. FTIR analyses show pronounced OH-stretching bands that indicate the presence of significant amounts of lattice-bonded water in bridgmanite. The high-water concentration in bridgmanite is further applied to better understand dehydration melting by downward flow of transition zone materials at the topmost lower mantle.

## 2. Experiments

Single-crystal (Al,Fe)-bearing bridgmanite with run number 5K2667 was synthesized at 24 GPa and 1800 °C using a Kawai-type cell at the Institute for Planetary Materials at Okayama University. The cell was equipped with Fujillo F08 tungsten carbide anvils with 6-mm truncation edge length and sintered  $\text{MgO-Cr}_2\text{O}_3$  pressure media with an octahedral edge length of 14 mm (Okuchi et al., 2015). Pressure calibration for this assembly was well established in previous studies (Shatskiy et al., 2009; Shatskiy et al., 2011). Starting sample mixture, including magnesium hydroxide [ $\text{Mg}(\text{OH})_2$ ], enstatite [ $\text{MgSiO}_3$ ], aluminum oxide [ $\text{Al}_2\text{O}_3$ ], and iron oxide [ $^{57}\text{FeO}$ ] in weight percentages of 21.6, 58.8, 11.8, and 7.8 wt%, respectively, were cold sealed into a Pt capsule, placed into the experimental assembly, and then compressed to ~24 GPa. The

capsule was then heated up to  $\sim 1800$  °C by supplying an electric power of 580 watts to the  $\text{LaCrO}_3$  heater. Under these P-T conditions, the sample mixture melted (Kawamoto, 2004) and bridgmanite crystals grew from the hydrous melt that initially contained  $\sim 6.7$  wt% water (see supporting information). Preestablished power-temperature relations from literature (Okuchi et al., 2015) were used to control the temperature in the sample capsule within approximately  $\pm 6\%$  uncertainty. We used a long heating duration of  $\sim 20$  hr to allow slow growth and formation of large and chemically homogenous bridgmanite crystals (Okuchi et al., 2015). This slow growth method is distinct from earlier studies using fast growth with large temperature gradients (Shatskiy et al., 2009; Shatskiy et al., 2011) or short-heating duration method (e.g., Meade et al., 1994; Murakami et al., 2002), which could result in hydrous inclusions in bridgmanite crystals. At the end of the synthesis, the electric power was shut down to quench the sample capsule to room temperature. In the decompressed and recovered sample capsule, large subhedral bridgmanite crystals with maximum grain sizes of  $\sim 400$   $\mu\text{m}$  in length were embedded in fine ground powder matrix (Figure 1a). The bridgmanite crystals display a light brownish color and can be easily extracted out from the surrounding matrix (Figure 1b).

Bridgmanite crystals and the matrix were initially analyzed with micro-Raman spectroscopy (see experimental details in supporting information). Collected Raman spectra in our bridgmanite crystals show sharp peaks at  $\sim 250$ ,  $\sim 280$ ,  $\sim 377$ , and  $\sim 496$   $\text{cm}^{-1}$  that are consistent with reported vibrational bands in  $\text{MgSiO}_3$  bridgmanite (Figures 1c and 1d; Durben & Wolf, 1992; Hemley et al., 1989). Some broad peaks at  $\sim 574$ ,  $\sim 709$ ,  $\sim 734$ , and  $\sim 881$   $\text{cm}^{-1}$  are probably due to the Fe and Al chemical substitutions (Litasov et al., 2003). On the other hand, the quenched matrix (Figures 1c and 1d) displays sharp Raman peaks at  $\sim 213$ ,  $\sim 329$ , and  $\sim 1,094$   $\text{cm}^{-1}$  that could be attributed to super hydrous phase B (Hofmeister et al., 1999; Ohtani et al., 2001), while the peak at  $\sim 3,640$   $\text{cm}^{-1}$  is characteristic of brucite phase (Bolfan-Casanova et al., 2003; Duffy et al., 1995). Overall, micro-Raman results show that the quenched ground matrix contains predominantly brucite and super hydrous phase B. Additionally, XRD analyses show these two phases in the ground matrix make up approximately 50% and 50%, respectively (Figure S1). We should note that the super hydrous phase B and brucite in the powder matrix were formed from residual melt during high-temperature quenching. Our synthesized bridgmanite crystals do not show any signatures of hydrous inclusions within the spectral and spatial resolution of micro-Raman spectroscopy.

The synthesized bridgmanite was further characterized using EPMA, Mössbauer spectroscopy, SEM-EDS mapping, synchrotron XRD, electron diffraction, and TEM analyses (see experimental details in Text S1 in supporting information). Combination of Mössbauer and EPMA results shows the crystals have an average chemical formula of  $\text{Mg}_{0.88}\text{Fe}^{3+}_{0.065}\text{Fe}^{2+}_{0.035}\text{Al}_{0.14}\text{Si}_{0.90}\text{O}_3$ , on the basis of three oxygen atoms within experimental uncertainties (Figure S2 and Table S1). Further SEM-EDS mapping of Fe, Al, Si, Mg, and O shows a chemically homogeneous single-crystal sample in micrometer-scale resolution (Figure S3a). Analyses of synchrotron XRD patterns at ambient conditions show the sample crystallizes in the *Pbnm* space group with refined unit cell parameters of  $a = 4.7875(3)$  Å,  $b = 4.9423(2)$  Å,  $c = 6.9205(6)$  (Figures 2a and 2b). Average full width at half maximum (FWHM) of integrated peaks is  $\sim 0.040^\circ$ , indicating high-quality crystallinity of synthesized bridgmanite. Additionally, collected selected area electron diffraction patterns on crystals in [221] and [121] zone axes confirmed its high-quality crystallinity without extra reflections (Figure 2c; Kojitani et al., 2007). We note that the refined unit cell parameters from selected area electron diffraction patterns are consistent with synchrotron XRD measurements within 1% accuracy. Further observations on a double-side polished crystal of  $\sim 30$ - $\mu\text{m}$  thick with a petrographic microscope confirmed no apparent inclusions or twinning of the sample (Figure S3b). In order to examine the quality of crystals in nanometer-scale resolution, HRTEM images were collected and simulated using EMS package (Stadelmann, 1987) over a wide range of thickness-defocus conditions to resolve the best fits (Figure S4). HRTEM results show that bridgmanite crystals have no visible inclusions or precipitates in nanometer-scale resolution but exhibit high density of structural defects (Figure 2d), which were probably due to Fe/Al substitution in the lattice and/or stress from high pressure-temperature quenching.

For FTIR and NanoSIMS measurements, we selected several pieces of big crystals,  $\sim 100$   $\mu\text{m}$  in length, with clear subhedral shapes, and double-side polished them to a thickness of 20–25  $\mu\text{m}$  using 3M diamond films. The thickness of each platelet was measured under a scaled stereo microscope with an accuracy of  $\pm 2$   $\mu\text{m}$ . To reliably determine their crystallographic orientations, synchrotron single-crystal XRD was conducted on

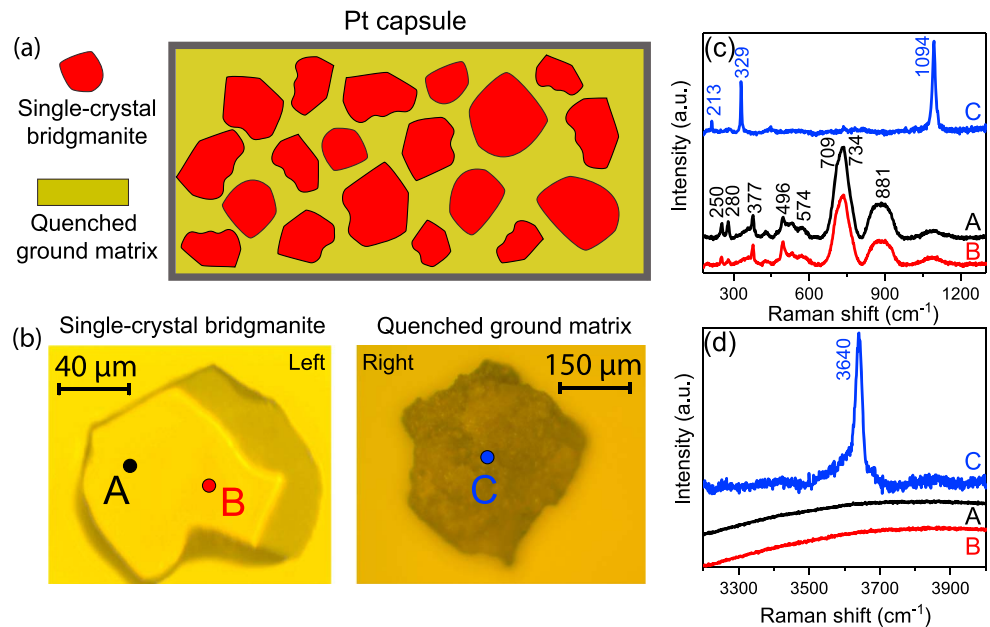


**Figure 1.** Sample synthesis and micro-Raman characterizations of quenched products in the Pt capsule. (a) Schematic figure of the recovered capsule with large subhedral bridgmanite crystals (red) and ground matrix (light green). Large-size single-crystal bridgmanite grew from the hydrous melt at high P-T conditions over a 20-hr heating duration with a slow growth rate. After high-temperature quenching, the residual melt turned into ground matrix containing super hydrous phase B and brucite, which surrounded the bridgmanite crystals. (b) Optical stereo microscope images of the recovered and polished bridgmanite crystal and quenched ground matrix using both transmitted and reflected lights. Selected areas of the bridgmanite crystal and ground matrix for Raman measurements are labeled as dots A, B, and C. (c and d) Collected Raman spectra of selected areas at micro-Raman shift ranges of 200–1,300 and 3,200–4,000  $\text{cm}^{-1}$ , respectively. Vibrational bands of bridgmanite are labeled with respective Raman frequency shifts (black). Raman spectra from ground matrix show sharp vibrational bands (labeled with blue), including the distinct OH-stretching at 3,640  $\text{cm}^{-1}$ .

platelets with rotations by  $\pm 16^\circ$  about the vertical axis of the sample stage. Two platelets with crystallographic orientations of  $(-0.50, 0.05, -0.86)$  and  $(0.16, 0.13, -0.98)$ , where the numbers correspond to the direction cosines in the crystallographic coordinates, denoted as P1 and P2 platelets, respectively, were used for measurements (Figure S5). We note that these two platelets were chosen due to the large surface areas after polishing and a dihedral angle of  $\sim 53.6^\circ$  between them that is sufficient to display the orientation effects, if any are present.

Unpolarized and polarized FTIR experiments were conducted on selected platelets before NanoSIMS measurements, because FTIR is nondestructive to the sample while NanoSIMS is destructive. FTIR experiments were performed at Yale University using a Varian 600 UMA FTIR spectrometer. The crystals were cleaned multiple times using acetone to remove potential contaminants from epoxy, and potential acetone left on the crystal surface were then removed using ethanol multiple times. To minimize possible noise, dry air was flushed into the FTIR spectrometer installation room, which reduced the detectable water content down to the lowest level of  $\sim 1$  ppm wt (Dai & Karato, 2009). Unpolarized infrared spectra were taken on the sample with 2,048 scans from 550 to 8,000  $\text{cm}^{-1}$  with a spectral resolution of 2  $\text{cm}^{-1}$  (Figure 3a). An aperture of  $50 \times 50 \mu\text{m}$  was used for the data collection. The obtained spectra were corrected by a linear baseline between 3,000 and 3,780  $\text{cm}^{-1}$ , which were used to calculate the absorbance. Additionally, polarized FTIR spectra were collected from the P1 platelet by rotating about its normal axis at an azimuthal angle of  $10^\circ$  apart (Figures 3b and S6).

After FTIR experiments, identical crystal platelets were sent to Department of Terrestrial Magnetism, Carnegie Institution for Science for NanoSIMS analyses using a Cameca NanoSIMS 50L. Three basaltic glass standards with known volatile concentrations were analyzed for calibrations before each analytical session (Lloyd et al., 2014). Presputtering was conducted on each spot using a  $10 \times 10 \mu\text{m}$  raster to remove potential

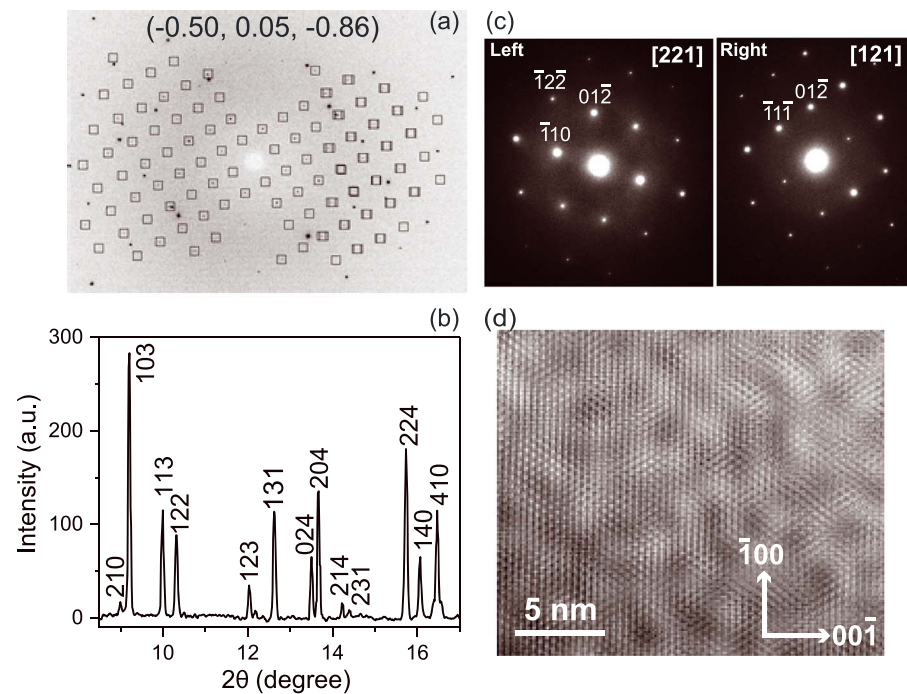


**Figure 2.** X-ray diffraction and transmission electron microscopy analyses of single-crystal bridgmanite. (a) A representative XRD image of the crystal with the orientation matrix determined using GSE-ADA/RSV software (Dera et al., 2013). (b) Integrated XRD pattern with main diffraction peaks labeled with identified miller indices (hkl). Integrated XRD peaks show an average FWHM of  $\sim 0.040^\circ$ . The wavelength of the incident X-ray beam was  $0.3344 \text{ \AA}$ . (c) Collected electron diffraction patterns in  $[221]$  (left) and  $[121]$  (right) zone axes. Miller indices (hkl) were labeled close to representative diffraction spots. (d) Fourier-filtered high-resolution transmission electron microscopy image of the single-crystal bridgmanite in the  $[010]$  zone axis.

surface contaminants. After the presputter, the area of the raster was reduced to  $7.5 \times 7.5 \mu\text{m}$  for NanoSIMS analyses. Following the procedure in literatures (Hauri et al., 2011; Lloyd et al., 2014), three to four spots were selected on each platelet for NanoSIMS measurements on hydrogen and other volatile elements, C, S, F, and Cl (Figures 3c and 3d).

### 3. Results and Discussion

In collected unpolarized spectra (Figure 3a), both platelets display two pronounced absorption bands centered at  $\sim 3,210$  and  $\sim 3,465 \text{ cm}^{-1}$  for P1 platelet and at  $\sim 3,230$  and  $\sim 3,475 \text{ cm}^{-1}$  for P2 platelet with an average FWHM of  $\sim 120 \text{ cm}^{-1}$ . Comparing with literature reports on  $\text{MgSiO}_3$ , Al-bearing and (Al,Fe)-bearing bridgmanite (Litasov et al., 2003), we could notice that a broad peak centered at  $3,400 \text{ cm}^{-1}$  with FWHM of  $\sim 250 \text{ cm}^{-1}$  was typically observed in FTIR spectra (Figure S7 and Table S2). An additional weak peak centered at  $\sim 3,100\text{--}3,200 \text{ cm}^{-1}$  also existed in (Al,Fe)-bearing bridgmanite in both MORB and peridotite systems (Litasov et al., 2003). Thus, the two absorption bands centered at approximately  $3,210\text{--}3,230$  and  $3,465\text{--}3,475 \text{ cm}^{-1}$  observed in our bridgmanite crystals could be assigned to be OH-stretching bands. Polarized FTIR spectra of P1 platelet show similar peak positions but significant intensity variations, especially for the band at  $\sim 3,210\text{--}3,230 \text{ cm}^{-1}$ , indicating a strong polarization effect (Figures 3b and S6). We note that the orientation of a single-crystal platelet could affect not only absorbance intensities but also band positions, resulting in offsets of peak positions and intensities between platelets (Jacobsen et al., 2005). We should note that in brucite two OH-stretching bands were found to be sharp with FWHM less than  $50 \text{ cm}^{-1}$  and centered at  $3,240$  and  $3,698 \text{ cm}^{-1}$  (Frost & Klopogge, 1999), while in super hydrous phase B, two IR bands at  $3,347$  and  $3,407 \text{ cm}^{-1}$  or one relatively broader band at  $3,373 \text{ cm}^{-1}$  were observed for low-temperature ordered or high-temperature disordered polymorphs, respectively (Koch-Müller et al., 2005). The IR bands from brucite and super

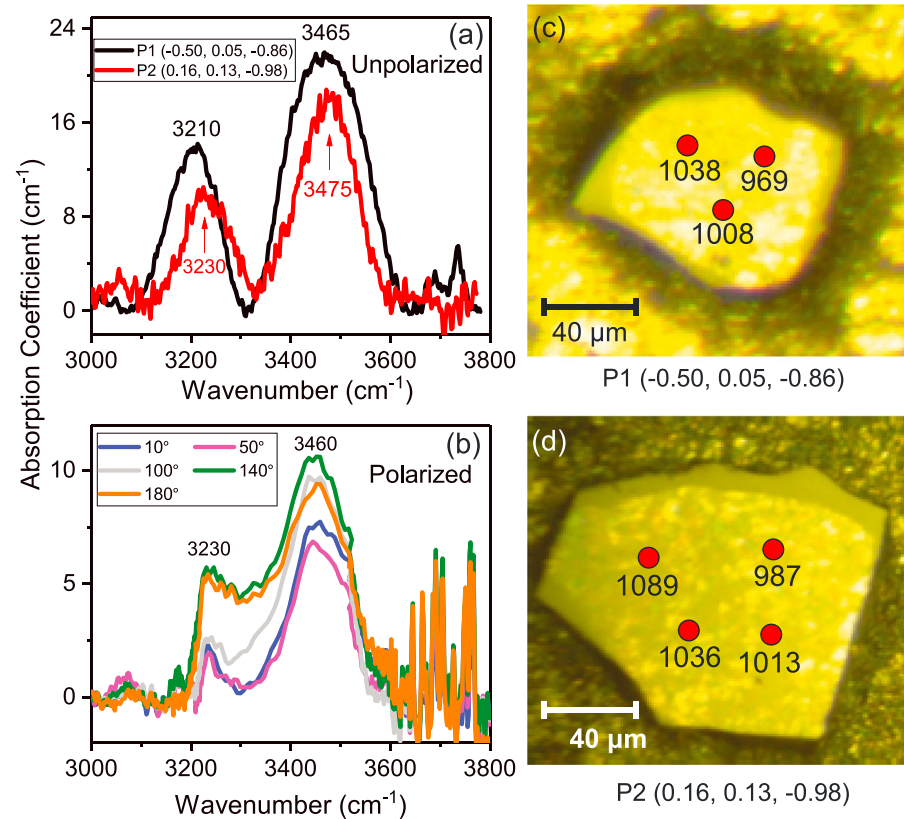


**Figure 3.** FTIR and NanoSIMS results on two single-crystal (Al,Fe)-bearing bridgmanite platelets with crystallographic orientations of  $(-0.50, 0.05, -0.88)$  (P1) and  $(0.16, 0.13, -0.98)$  (P2). (a) Representative unpolarized IR spectra of P1 and P2 platelets. Two IR absorption bands are observed for both platelets, centering at  $\sim 3,210$  and  $\sim 3,465$   $\text{cm}^{-1}$  for P1 and at  $\sim 3,230$  and  $\sim 3,475$   $\text{cm}^{-1}$  for P2. Thickness of both platelets is  $\sim 20$   $\mu\text{m}$ . (b) Representative polarized IR spectra of P1 platelet at different azimuthal angles. The angles represent the rotation of the crystal platelet about its normal axis. Numbers in (a) and (b) next to peaks show OH-stretching frequencies with a unit of  $\text{cm}^{-1}$ . (c) and (d) Optical images of P1 and P2 platelets in Ir holders under reflected light. The images were taken right before NanoSIMS analyses. Three to four areas labeled as red dots were selected for NanoSIMS measurements. Numbers next to red dots represent determined water concentrations in ppm wt.

hydrous phase B are not observed in measured FTIR spectra, indicating no such hydrous inclusions in our bridgmanite crystals within the spectral resolution of FTIR measurements.

Reliable calibrations for absorption coefficients and orientation factors of bridgmanite crystals in FTIR spectra analyses have yet to be established at this point in time. This has prevented us and all the other previous investigators to reliably evaluate the water concentrations in bridgmanite with or without Fe/Al substitution. In order to roughly estimate the hydrogen concentration from FTIR spectra, we followed the calibration method of Paterson (1982). After appropriate subtraction of baselines, the water content could be calculated using the equation:

$$C_{\text{OH}} = \frac{X_i}{150\xi} \int \frac{k(\bar{\nu})}{(3780 - \bar{\nu})} d\bar{\nu}$$

where  $C_{\text{OH}}$  has a unit of ppm wt water;  $X_i$  is the density factor in cm ppm wt water, calculated as  $X_i = 10^6 \times (18/2d)$  with  $d$  as the mineral density of 4,200 g/L, and  $X_i$  is calculated to be 2,142 cm ppm wt water for the (Al,Fe)-bearing bridgmanite used here;  $k(\bar{\nu})$  is the absorption coefficient in  $\text{cm}^{-1}$  for a given wavenumber ( $\bar{\nu}$ ) as shown in Figure 3a;  $\xi$  is the orientation factor that is assumed as 1/3 for unpolarized spectra. The value of 1/3 for  $\xi$  is taken from literatures on relatively better investigated upper-mantle minerals (e.g., Jacobsen et al., 2005) under the assumption that mineral grains were randomly oriented under unpolarized light.

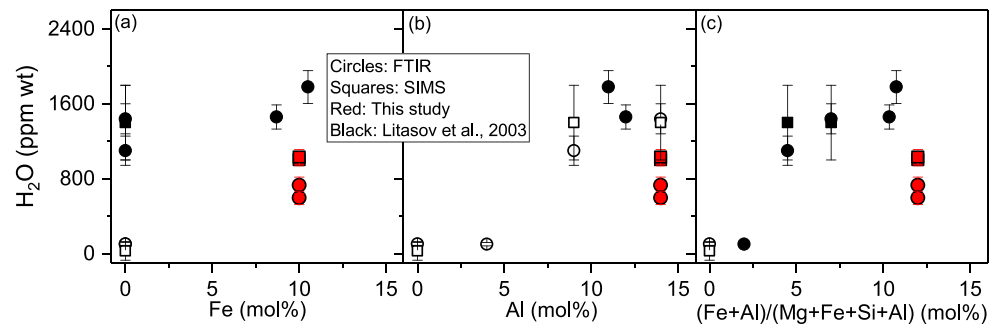


**Figure 4.** Comparison of water concentrations in bridgmanite with different Fe and Al contents from this study and Litasov et al. (2003). Data sets in literatures (Bolfan-Casanova et al., 2003; Inoue et al., 2010; Murakami et al., 2002; Panero et al., 2015) are tabulated in Table S2 but excluded in the plot because of possible contaminations and/or influences by coexisting phase(s). (a) Water concentrations as a function of Fe content (mol%) in bridgmanite; (b) Water concentrations as a function of Al content (mol%) in bridgmanite; (c) Water concentrations as a function of average Fe and Al contents (mol%) in bridgmanite, calculated as  $(\text{Fe} + \text{Al})/(\text{Mg} + \text{Fe} + \text{Si} + \text{Al})$ . Circles are data from FTIR measurements and squares are results from SIMS/NanoSIMS measurements. Symbols are used to distinguish the effects of Fe and Al in bridgmanite: (a) open and solid symbols are Al-free and Al-bearing bridgmanite, respectively; (b) open and solid symbols are Fe-free and Fe-bearing bridgmanite, respectively; and (c) open and solid symbols are endmember  $\text{MgSiO}_3$  and (Al,Fe)-bearing bridgmanite, respectively. FTIR = Fourier-transform infrared; SIMS = secondary ion mass spectrometry.

Under these conditions, water concentrations in P1 and P2 platelets were calculated as  $731(\pm 68)$  and  $596(\pm 53)$  ppm wt, respectively (Table S2).

NanoSIMS measurements show the average water concentration is about  $1,020(\pm 70)$  ppm wt for both platelets (Figures 3c and 3d). The variations of measured water concentration in different spots of the platelets are typically less than 70 ppm wt at  $\pm 2\sigma$  level. All the other volatile elements (C, S, F, and Cl) are less than 1 ppm wt, indicating minimal contaminations from epoxy or residual hydrocarbons (e.g., acetone) on the surface.

Our results show that the measured water concentrations from NanoSIMS are similar but greater than the estimated values from FTIR. Literature studies indicate that SIMS analyses commonly result in higher water concentrations in minerals than FTIR (e.g., Mosenfelder et al., 2015). Bolfan-Casanova et al. (2003) stated a possible reason that SIMS cannot discriminate hydrogen counts from microscopic inclusions within samples. Such contaminations cannot be ruled out in previous studies (Bolfan-Casanova et al., 2000; Bolfan-Casanova et al., 2003; Litasov et al., 2003; Murakami et al., 2002; Panero et al., 2015). We note that the collected HRTEM images on our bridgmanite crystals can be used to exclude the possibility that precipitation of water or hydrous inclusions were captured within the crystal in nanometer-scale resolution. Thus, we argue that such inconsistency between FTIR and NanoSIMS could come from the FTIR data analysis procedure, where  $\xi$  was simply assumed as 1/3 due to the lack of such information. Early studies indicate that  $\xi$  can be affected by many factors including the nature of spectra, thickness of the sample, and degree of polarization anisotropy (Bell et al., 2003). They also show that the use of calibration method by Paterson (1982) to analyze unpolarized IR data on oriented olivine crystal platelets would underestimate its water concentration by 2.3–3.5 times due to the choice of  $\xi$  (Bell et al., 2003). Due to the lack of reliable calibration of  $\xi$  for bridgmanite, we believe the roughly calculated 600–730 ppm wt water from FTIR analyses should be an underestimate for the water concentration in our bridgmanite crystals. Considering the well-characterized high-quality nature of bridgmanite crystals used here, the results from NanoSIMS should represent a reliable characterization of its lattice-bonded water. The strong OH-stretching bands in FTIR spectra provide supportive evidence of its high water concentration.

A comparison between previous experimental observations (e.g., Litasov et al., 2003; Meade et al., 1994) and this study shows that, for the first order, water concentrations in bridgmanite increase with increasing Fe and/or Al contents (Figure 4). We note that some data sets in the literatures (Bolfan-Casanova et al., 2003; Inoue et al., 2010; Murakami et al., 2002; Panero et al., 2015) are excluded in the comparison because water contents in these studies could be contaminated by inclusions and/or coexisting phases. We speculate that hydrogen substitution in bridgmanite involves a link to Fe and/or Al substitution. Two hydrogen substitution mechanisms have been proposed to link the high water concentrations in Al-bearing bridgmanite

(Litasov et al., 2003): (1) cation vacancy associated with  $\text{Al}^{3+}$  substitution at the Si site via  $\text{Si}^{4+} \leftrightarrow \text{Al}^{3+} + \text{H}^+$  (e.g., Hernández et al., 2013) and (2) interstitial sites associated with oxygen vacancies  $2\text{Si}^{4+} \leftrightarrow 2\text{Al}^{3+} + \text{V}_\text{O}$ , which can be hydrated via  $\text{V}_\text{O} + \text{O}^{2-} + \text{H}_2\text{O} \leftrightarrow 2\text{OH}^-$  (Litasov et al., 2003; Navrotsky, 1999). Both mechanisms result in  $\text{Al}^{3+}$  in the Si site, which attracts protons and could explain the enhanced hydrogen solubility in Al-bearing bridgmanite. In either case, there will be a volume expansion.

With the limited data presented here, it is difficult to constrain hydrogen substitution mechanism in our bridgmanite crystals at an atomistic level, but the peak frequencies in FTIR spectra represent the strength of OH-stretching bands that could help us identify the relevant location of hydrogen (e.g., Balan et al., 2008; Jacobsen et al., 2005; Tollan et al., 2017). Previous studies on olivine (e.g., Balan et al., 2008; Tollan et al., 2017) provide a hint for assigning the two absorption peaks observed here to possible mechanisms: the peak at  $\sim 3,460 \text{ cm}^{-1}$  might correspond to hydrogen substitution associated with  $\text{Al}^{3+}$  (Si site) and the other one at  $\sim 3,230 \text{ cm}^{-1}$  might correspond to hydrogen trapped in the Mg-site vacancy (Table S2; e.g., Balan et al., 2008; Tollan et al., 2017). The former is consistent with the model of  $\text{Al}^{3+}$  incorporation in the Si site in bridgmanite (e.g., Hernández et al., 2013; Litasov et al., 2003; Navrotsky, 1999), while the latter is consistent with  $\text{Fe}^{3+}$  mainly substituting in the Mg site, as revealed by our Mössbauer spectroscopy results. This substitution would promote the formation of Mg-site vacancies.

#### 4. Geophysical Implication

Bridgmanite and ferropericlase are the two most abundant minerals in the Earth's lower mantle, comprising of about 75 and 18 vol% of the region, respectively (Irifune et al., 2010; Ringwood, 1975). Extensive experiments (Bolfan-Casanova et al., 2002; Bolfan-Casanova et al., 2006; Joachim et al., 2013; Litasov, 2010) and ab initio calculations (Merli et al., 2016; Muir & Brodholt, 2018) show that the water concentration in ferropericlase is rather limited within the range of 10–80 ppm wt. These studies also suggest that water in the lower mantle prefers to exist in (Al,Fe)-bearing bridgmanite. Taking into account deep-mantle compositional models (Irifune et al., 2010; Ringwood, 1975), our (Al,Fe)-bearing bridgmanite could be representative of the Fe, Al, and  $\text{Fe}^{3+}/\Sigma\text{Fe}$  ( $\sim 0.65$ ) contents in the lower mantle (Frost et al., 2004; McCammon, 1997). The high water concentration,  $\sim 1,020 (\pm 70)$  ppm wt, suggests that in comparison to ferropericlase, (Al,Fe)-bearing bridgmanite should be the main water carrier in the lower mantle.

The high water concentration in lower-mantle bridgmanite could greatly affect its chemical and physical properties. The most direct and important effect is likely the influence on melting. Seismic low-velocity observations at the topmost lower mantle (below 660-km discontinuity) has been attributed to dehydration melting of hydrous ringwoodite transitioning to bridgmanite (e.g., Liu et al., 2016; Liu et al., 2018; Schmandt et al., 2014). Previous studies on water content in the transition zone have been controversial, but an estimate from an electrical conductivity study (Karato, 2011) shows  $\sim 0.1$  wt% on average with large regional variations. Our findings show that  $\sim 0.1$  wt% water could be dissolved into bridgmanite (the water content in solidus) with the coexisting melt containing  $\sim 13$ – $18$  wt% water (the water content in liquidus; the range reflects possible uncertainties in the estimate) at approximately 24 GPa and 1800 °C (see Text S3 in supporting information). The P-T conditions at 660-km depth are expected to be  $\sim 23.6$  GPa and  $\sim 1600$  °C (Katsura et al., 2010), where bridgmanite would likely be able to accommodate slightly more water than what we observed here. These observations indicate that for dehydration melting to occur at the topmost lower mantle near the 660-km depth, the water concentration in downward flow of transition zone materials must exceed the solubility limit of about 0.1 wt%. When dehydration melting occurs, the melt will contain a large amount of water at the topmost lower mantle and hence likely affect the characteristics of seismic waves and contribute to the nature of global water circulation (Liu et al., 2016; Liu et al., 2018).

We note that the bridgmanite crystals in this study were synthesized at relatively shallow lower-mantle P-T conditions. To understand water concentration and possible dehydration mechanism in deeper parts of lower mantle, extrapolation to higher P-T conditions needs to be taken into account but with great care. Hydrogen dissolved into bridgmanite might affect its plastic deformation (diffusion) and electrical conductivity. However, the magnitude of hydrogen substitution effects on these properties for bridgmanite is poorly constrained at this time. High P-T experimental studies on the effects of hydrogen in bridgmanite are crucially needed to better understand the dynamic process of Earth's lower mantle.

## Acknowledgments

The authors thank Z. Jiang for his assistance with FTIR measurements at Yale University and a discussion on TEM results. The authors thank C. McCammon for helping with Mössbauer spectroscopy data collection and data analysis on the bridgmanite crystals. We acknowledge V. Prakapenka for the assistance with X-ray diffraction experiments at 13ID-D, GSECARS. GSECARS operations are supported by the National Science Foundation-Earth Sciences (EAR-1128799) and the U.S. Department of Energy, Geosciences (DE-FG02-94ER14466). J. F. L. acknowledges support from National Science Foundation Geophysics Program (EAR-1446946 & EAR-1916941) and Deep Carbon Observatory of the Sloan Foundation. S. K. acknowledges support from EAR-1082622. A. G. G. acknowledges support of RScF 16-12-10464 grant and Center for Collective Use "Accelerator Center for Neutron Research of the Structure of Substance and Nuclear Medicine" of the INR RAS. TEM analyses were supported by the Ministry of Science and Higher Education within the State assignment FSRC «Crystallography and Photonics» RAS. Experimental data for EPMA are listed in Table S1. Raw unpolarized and polarized FTIR data are available in the supporting information. All the data to produce all the figures in this paper are available on Zenodo (<http://doi.org/10.5281/zenodo.3364107>). More detailed information of experimental results can be found in the supporting information.

## References

- Asimov, P. D., Stein, L. C., Mosenfelder, J. L., & Rossman, G. R. (2006). Quantitative polarized infrared analysis of trace OH in populations of randomly oriented mineral grains. *American Mineralogist*, *91*(2-3), 278–284. <https://doi.org/10.2138/am.2006.1937>
- Aubaud, C., Withers, A. C., Hirschmann, M. M., Guan, Y., Leshin, L. A., Mackwell, S. J., & Bell, D. R. (2007). Intercalibration of FTIR and SIMS for hydrogen measurements in glasses and nominally anhydrous minerals. *American Mineralogist*, *92*(5-6), 811–828. <https://doi.org/10.2138/am.2007.2248>
- Balan, E., Refson, K., Blanchard, M., Delattre, S., Lazzeri, M., Ingrin, J., et al. (2008). Theoretical infrared absorption coefficient of OH groups in minerals. *American Mineralogist*, *93*(5-6), 950–953. <https://doi.org/10.2138/am.2008.2889>
- Bell, D. R., Rossman, G. R., Maldener, J., Endisch, D., & Rauch, F. (2003). Hydroxide in olivine: A quantitative determination of the absolute amount and calibration of the IR spectrum. *Journal of Geophysical Research*, *108*(B2), 2105. <https://doi.org/10.1029/2001JB000679>
- Bercovici, D., & Karato, S.-i. (2003). Whole-mantle convection and the transition-zone water filter. *Nature*, *425*(6953), 39–44. <https://doi.org/10.1038/nature01918>
- Bolfan-Casanova, N. (2005). Water in the Earth's mantle. *Mineralogical Magazine*, *69*(3), 229–257. <https://doi.org/10.1180/0026461056930248>
- Bolfan-Casanova, N., Keppler, H., & Rubie, D. C. (2000). Water partitioning between nominally anhydrous minerals in the MgO–SiO<sub>2</sub>–H<sub>2</sub>O system up to 24 GPa: Implications for the distribution of water in the Earth's mantle. *Earth and Planetary Science Letters*, *182*(3-4), 209–221. [https://doi.org/10.1016/S0012-821X\(00\)00244-2](https://doi.org/10.1016/S0012-821X(00)00244-2)
- Bolfan-Casanova, N., Keppler, H., & Rubie, D. C. (2003). Water partitioning at 660 km depth and evidence for very low water solubility in magnesium silicate perovskite. *Geophysical Research Letters*, *30*(17), 1905. <https://doi.org/10.1029/2003GL017182>
- Bolfan-Casanova, N., Mackwell, S., Keppler, H., McCammon, C., & Rubie, D. (2002). Pressure dependence of H solubility in magnesiowüstite up to 25 GPa: Implications for the storage of water in the Earth's lower mantle. *Geophysical Research Letters*, *29*(10), 1449. <https://doi.org/10.1029/2001GL014457>
- Bolfan-Casanova, N., McCammon, C. A., & Mackwell, S. J. (2006). Water in transition zone and lower mantle minerals. In *Earth's Deep Water Cycle*, (pp. 57–68). Washington, DC: American Geophysical Union.
- Dai, L., & Karato, S.-i. (2009). Electrical conductivity of wadsleyite at high temperatures and high pressures. *Earth and Planetary Science Letters*, *287*(1-2), 277–283. <https://doi.org/10.1016/j.epsl.2009.08.012>
- Dera, P., Zhuravlev, K., Prakapenka, V., Rivers, M. L., Finkelstein, G. J., Grubor-Urošević, O., et al. (2013). High pressure single-crystal micro X-ray diffraction analysis with GSE\_ADA/RSV software. *High Pressure Research*, *33*(3), 466–484. <https://doi.org/10.1080/08957959.2013.806504>
- Duffy, T. S., Meade, C., Fei, Y., Mao, H.-K., & Hemley, R. J. (1995). High-pressure phase transition in brucite, Mg(OH)<sub>2</sub>. *American Mineralogist*, *80*(3-4), 222–230. <https://doi.org/10.2138/am-1995-3-403>
- Durben, D. J., & Wolf, G. H. (1992). High-temperature behavior of metastable MgSiO<sub>3</sub> perovskite: A Raman spectroscopic study. *American Mineralogist*, *77*(7-8), 890–893.
- Frost, D. J., Liebske, C., Langenhorst, F., McCammon, C. A., Trønnes, R. G., & Rubie, D. C. (2004). Experimental evidence for the existence of iron-rich metal in the Earth's lower mantle. *Nature*, *428*(6981), 409–412. <https://doi.org/10.1038/nature02413>
- Frost, R. L., & Klopogrog, J. T. (1999). Infrared emission spectroscopic study of brucite. *Spectrochimica Acta Part A: Molecular and Biomolecular Spectroscopy*, *55*(11), 2195–2205. [https://doi.org/10.1016/S1386-1425\(99\)00016-5](https://doi.org/10.1016/S1386-1425(99)00016-5)
- Hauri, E. H., Weinreich, T., Saal, A. E., Rutherford, M. C., & van Orman, J. A. (2011). High pre-eruptive water contents preserved in lunar melt inclusions. *Science*, *333*(6039), 213–215. <https://doi.org/10.1126/science.1204626>
- Hemley, R., Cohen, R., Yeganeh-Haeri, A., Mao, H., Weidner, D., & Ito, E. (1989). Raman spectroscopy and lattice dynamics of MgSiO<sub>3</sub>-perovskite at high pressure. *Perovskite: A Structure of Great Interest to Geophysics and Materials Science*, *45*, 35–44.
- Hernández, E. R., Alfe, D., & Brodholt, J. (2013). The incorporation of water into lower-mantle perovskites: A first-principles study. *Earth and Planetary Science Letters*, *364*, 37–43. <https://doi.org/10.1016/j.epsl.2013.01.005>
- Hofmeister, A., Cynn, H., Burnley, P., & Meade, C. (1999). Vibrational spectra of dense, hydrous magnesium silicates at high pressure: Importance of the hydrogen bond angle. *American Mineralogist*, *84*(3), 454–464. <https://doi.org/10.2138/am-1999-0330>
- Inoue, T. (1994). Effect of water on melting phase relations and melt composition in the system Mg<sub>2</sub>SiO<sub>4</sub>–MgSiO<sub>3</sub>–H<sub>2</sub>O up to 15 GPa. *Physics of the Earth and Planetary Interiors*, *85*(3-4), 237–263. [https://doi.org/10.1016/0031-9201\(94\)90116-3](https://doi.org/10.1016/0031-9201(94)90116-3)
- Inoue, T., Wada, T., Sasaki, R., & Yurimoto, H. (2010). Water partitioning in the Earth's mantle. *Physics of the Earth and Planetary Interiors*, *183*(1-2), 245–251. <https://doi.org/10.1016/j.pepi.2010.08.003>
- Irfune, T., Shinmei, T., McCammon, C. A., Miyajima, N., Rubie, D. C., & Frost, D. J. (2010). Iron partitioning and density changes of pyrolyte in Earth's lower mantle. *Science*, *327*(5962), 193–195. <https://doi.org/10.1126/science.1181443>
- Jacobsen, S. D., Demouchy, S., Frost, D. J., Ballaran, T. B., & Kung, J. (2005). A systematic study of OH in hydrous wadsleyite from polarized FTIR spectroscopy and single-crystal X-ray diffraction: Oxygen sites for hydrogen storage in Earth's interior. *American Mineralogist*, *90*(1), 61–70. <https://doi.org/10.2138/am.2005.1624>
- Joachim, B., Wohlers, A., Norberg, N., Gardés, E., Petrishcheva, E., & Abart, R. (2013). Diffusion and solubility of hydrogen and water in periclase. *Physics and Chemistry of Minerals*, *40*(1), 19–27. <https://doi.org/10.1007/s00269-012-0542-8>
- Kaminsky, F. V. (2018). Water in the Earth's lower mantle. *Geochemistry International*, *56*(12), 1117–1134. <https://doi.org/10.1134/S0016702918120042>
- Karato, S. (2015). Water in the evolution of the Earth and other terrestrial planets. *Treatise on Geophysics*, *9*, 105–144.
- Karato, S.-i. (2011). Water distribution across the mantle transition zone and its implications for global material circulation. *Earth and Planetary Science Letters*, *301*(3-4), 413–423. <https://doi.org/10.1016/j.epsl.2010.11.038>
- Karato, S.-I., & Jung, H. (2003). Effects of pressure on high-temperature dislocation creep in olivine. *Philosophical Magazine*, *83*(3), 401–414. <https://doi.org/10.1080/0141861021000025829>
- Karato, S.-i., & Wang, D. (2013). Electrical conductivity of minerals and rocks. *Physics and Chemistry of the Deep Earth*, 145–182. <https://doi.org/10.1002/9781118529492.ch5>
- Katsura, T., Yoneda, A., Yamazaki, D., Yoshino, T., & Ito, E. (2010). Adiabatic temperature profile in the mantle. *Physics of the Earth and Planetary Interiors*, *183*(1-2), 212–218. <https://doi.org/10.1016/j.pepi.2010.07.001>
- Kawamoto, T. (2004). Hydrous phase stability and partial melt chemistry in H<sub>2</sub>O-saturated KLB-1 peridotite up to the uppermost lower mantle conditions. *Physics of the Earth and Planetary Interiors*, *143*, 387–395.

- Koch-Müller, M., Dera, P., Fei, Y., Hellwig, H., Liu, Z., van Orman, J., & Wirth, R. (2005). Polymorphic phase transition in superhydrous phase B. *Physics and Chemistry of Minerals*, *32*(5-6), 349–361. <https://doi.org/10.1007/s00269-005-0007-4>
- Kojitani, H., Katsura, T., & Akaogi, M. (2007). Aluminum substitution mechanisms in perovskite-type  $\text{MgSiO}_3$ : An investigation by Rietveld analysis. *Physics and Chemistry of Minerals*, *34*(4), 257–267. <https://doi.org/10.1007/s00269-007-0144-z>
- Kumamoto, K. M., Warren, J. M., & Hauri, E. H. (2017). New SIMS reference materials for measuring water in upper mantle minerals. *American Mineralogist*, *102*(3), 537–547. <https://doi.org/10.2138/am-2017-5863CCBYNCND>
- Litasov, K. (2010). The influence of  $\text{Al}_2\text{O}_3$  on the  $\text{H}_2\text{O}$  content in periclase and ferropericlase at 25 GPa. *Russian Geology and Geophysics*, *51*(6), 644–649. <https://doi.org/10.1016/j.rgg.2010.05.005>
- Litasov, K., Ohtani, E., Langenhorst, F., Yurimoto, H., Kubo, T., & Kondo, T. (2003). Water solubility in Mg-perovskites and water storage capacity in the lower mantle. *Earth and Planetary Science Letters*, *211*(1-2), 189–203. [https://doi.org/10.1016/S0012-821X\(03\)00200-0](https://doi.org/10.1016/S0012-821X(03)00200-0)
- Litasov, K. D., Kagi, H., Shatskiy, A., Ohtani, E., Lakshtanov, D. L., Bass, J. D., & Ito, E. (2007). High hydrogen solubility in Al-rich stishovite and water transport in the lower mantle. *Earth and Planetary Science Letters*, *262*(3-4), 620–634. <https://doi.org/10.1016/j.epsl.2007.08.015>
- Liu, Z., Park, J., & Karato, S. I. (2016). Seismological detection of low-velocity anomalies surrounding the mantle transition zone in Japan subduction zone. *Geophysical Research Letters*, *43*, 2480–2487. <https://doi.org/10.1002/2015GL067097>
- Liu, Z., Park, J., & Karato, S.-i. (2018). Seismic evidence for water transport out of the mantle transition zone beneath the European Alps. *Earth and Planetary Science Letters*, *482*, 93–104. <https://doi.org/10.1016/j.epsl.2017.10.054>
- Lloyd, A. S., Ruprecht, P., Hauri, E. H., Rose, W., Gonnermann, H. M., & Plank, T. (2014). NanoSIMS results from olivine-hosted melt embayments: Magma ascent rate during explosive basaltic eruptions. *Journal of Volcanology and Geothermal Research*, *283*, 1–18. <https://doi.org/10.1016/j.jvolgeores.2014.06.002>
- McCammon, C. (1997). Perovskite as a possible sink for ferric iron in the lower mantle. *Nature*, *387*(6634), 694–696. <https://doi.org/10.1038/42685>
- Meade, C., Reffner, J. A., & Ito, E. (1994). Synchrotron infrared absorbance measurements of hydrogen in  $\text{MgSiO}_3$  perovskite. *Science*, *264*(5165), 1558–1560. <https://doi.org/10.1126/science.264.5165.1558>
- Mei, S., & Kohlstedt, D. (2000). Influence of water on plastic deformation of olivine aggregates: 1. Diffusion creep regime. *Journal of Geophysical Research*, *105*(B9), 21,457–21,469. <https://doi.org/10.1029/2000JB900179>
- Merli, M., Bonadiman, C., Diella, V., & Pavese, A. (2016). Lower mantle hydrogen partitioning between periclase and perovskite: A quantum chemical modelling. *Geochimica et Cosmochimica Acta*, *173*, 304–318. <https://doi.org/10.1016/j.gca.2015.10.025>
- Mosenfelder, J. L., le Voyer, M., Rossman, G. R., Guan, Y., Bell, D. R., Asimow, P. D., & Eiler, J. M. (2011). Analysis of hydrogen in olivine by SIMS: Evaluation of standards and protocol. *American Mineralogist*, *96*(11-12), 1725–1741. <https://doi.org/10.2138/am.2011.3810>
- Mosenfelder, J. L., Rossman, G. R., & Johnson, E. A. (2015). Hydrous species in feldspars: A reassessment based on FTIR and SIMS. *American Mineralogist*, *100*(5-6), 1209–1221. <https://doi.org/10.2138/am-2015-5034>
- Muir, J. M., & Brodholt, J. P. (2018). Water distribution in the lower mantle: Implications for hydrolytic weakening. *Earth and Planetary Science Letters*, *484*, 363–369. <https://doi.org/10.1016/j.epsl.2017.11.051>
- Murakami, M., Hirose, K., Yurimoto, H., Nakashima, S., & Takafuji, N. (2002). Water in Earth's lower mantle. *Science*, *295*(5561), 1885–1887. <https://doi.org/10.1126/science.1065998>
- Navrotsky, A. (1999). A lesson from ceramics. *Science*, *284*(5421), 1788–1789. <https://doi.org/10.1126/science.284.5421.1788>
- Ohtani, E. (2015). Hydrous minerals and the storage of water in the deep mantle. *Chemical Geology*, *418*, 6–15. <https://doi.org/10.1016/j.chemgeo.2015.05.005>
- Ohtani, E., Toma, M., Litasov, K., Kubo, T., & Suzuki, A. (2001). Stability of dense hydrous magnesium silicate phases and water storage capacity in the transition zone and lower mantle. *Physics of the Earth and Planetary Interiors*, *124*(1-2), 105–117. [https://doi.org/10.1016/S0031-9201\(01\)00192-3](https://doi.org/10.1016/S0031-9201(01)00192-3)
- Okuchi, T., Purejav, N., Tomioka, N., Lin, J.-F., Kuribayashi, T., Schoneveld, L., et al. (2015). Synthesis of large and homogeneous single crystals of water-bearing minerals by slow cooling at deep-mantle pressures. *American Mineralogist*, *100*(7), 1483–1492. <https://doi.org/10.2138/am-2015-5237>
- Panero, W. R., Pigott, J. S., Reaman, D. M., Kabbes, J. E., & Liu, Z. (2015). Dry (Mg, Fe)  $\text{SiO}_3$  perovskite in the Earth's lower mantle. *Journal of Geophysical Research: Solid Earth*, *120*, 894–908. <https://doi.org/10.1002/2014JB011397>
- Paterson, M. (1982). The determination of hydroxyl by infrared absorption in quartz, silicate glasses and similar materials. *Bulletin de Mineralogie*, *105*, 20–29.
- Pearson, D., Brenker, F., Nestola, F., McNeill, J., Nasdala, L., Hutchison, M., et al. (2014). Hydrous mantle transition zone indicated by ringwoodite included within diamond. *Nature*, *507*(7491), 221–224. <https://doi.org/10.1038/nature13080>
- Peslier, A. H., Schönbacher, M., Busemann, H., & Karato, S.-I. (2017). Water in the Earth's interior: Distribution and origin. *Space Science Reviews*, *212*(1-2), 743–810. <https://doi.org/10.1007/s11214-017-0387-z>
- A. E. Ringwood (1975), Composition and petrology of the Earth's mantle [by] AE Ringwood.
- Sambridge, M., Gerald, J. F., Kovács, I., O'Neill, H. S. C., & Hermann, J. R. (2008). Quantitative absorbance spectroscopy with unpolarized light: Part I. Physical and mathematical development. *American Mineralogist*, *93*(5-6), 751–764. <https://doi.org/10.2138/am.2008.2657>
- Schmandt, B., Jacobsen, S. D., Becker, T. W., Liu, Z., & Dueker, K. G. (2014). Dehydration melting at the top of the lower mantle. *Science*, *344*(6189), 1265–1268. <https://doi.org/10.1126/science.1253358>
- Schwager, B., Chudinovskikh, L., Gavriluk, A., & Boehler, R. (2004). Melting curve of  $\text{H}_2\text{O}$  to 90 GPa measured in a laser-heated diamond cell. *Journal of Physics: Condensed Matter*, *16*(14), S1177.
- Shatskiy, A., Katsura, T., Litasov, K., Shcherbakova, A., Borzdov, Y., Yamazaki, D., et al. (2011). High pressure generation using scaled-up Kawai-cell. *Physics of the Earth and Planetary Interiors*, *189*(1-2), 92–108. <https://doi.org/10.1016/j.pepi.2011.08.001>
- Shatskiy, A., Litasov, K. D., Matsuzaki, T., Shinoda, K., Yamazaki, D., Yoneda, A., et al. (2009). Single crystal growth of wadsleyite. *American Mineralogist*, *94*(8-9), 1130–1136. <https://doi.org/10.2138/am.2009.3150>
- Spektor, K., Nysten, J., Stoyanov, E., Navrotsky, A., Hervig, R. L., Leinenweber, K., et al. (2011). Ultrahydrous stishovite from high-pressure hydrothermal treatment of  $\text{SiO}_2$ . *Proceedings of the National Academy of Sciences*, *108*(52), 20,918–20,922. <https://doi.org/10.1073/pnas.1117152108>
- Stadelmann, P. (1987). EMS-a software package for electron diffraction analysis and HREM image simulation in materials science. *Ultramicroscopy*, *21*(2), 131–145. [https://doi.org/10.1016/0304-3991\(87\)90080-5](https://doi.org/10.1016/0304-3991(87)90080-5)

- Tauzin, B., Debayle, E., & Wittlinger, G. (2010). Seismic evidence for a global low-velocity layer within the Earth's upper mantle. *Nature Geoscience*, 3(10), 718–721. <https://doi.org/10.1038/ngeo969>
- Tollan, P. M., Smith, R., O'Neill, H. S. C., & Hermann, J. (2017). The responses of the four main substitution mechanisms of H in olivine to H<sub>2</sub>O activity at 1050 °C and 3 GPa. *Progress in Earth and Planetary Science*, 4(1), 14. <https://doi.org/10.1186/s40645-017-0128-7>